Molecular Dynamics Model of Ultraviolet Matrix-Assisted Laser Desorption/Ionization Including Ionization Processes

Richard Knochenmuss[*1] and Leonid V. Zhigilei[2]
1) Novartis Institutes for Biomedical Research
4056 Basel, Switzerland
and
2) Dept. of Materials Science and Engineering
116 Engineer's Way
University of Virginia
Charlottesville, Virginia
22904-4745, USA

Abstract

A molecular dynamics model of UV-MALDI including ionization processes is presented. In addition to the previously described breathing sphere approach developed for simulation of laser ablation/desorption of molecular systems, it includes radiative and non-radiative decay, exciton hopping, two pooling processes and electron capture. The results confirm the main conclusions of the continuum model of Knochenmuss, *Anal. Chem.* **2003**, *75*, 2199, but provide a much more detailed description of the interaction between ablation/desorption and ionization processes in the critical early time regime. Both desorption and ablation regimes generate free ions, and yields are in accordance with experiment. The first molecular ions are emitted at high velocities shortly before neutral desorption begins, due to surface charging caused by electron escape from the top of the sample. Later ions are entrained and thermalized in the plume of neutral molecules and clusters. Clusters are found to be stable on a nanosecond time scale, so the ions in them will be released only slowly, if at all. Exciton hopping rate and the mean radius for ion recombination are shown to be key parameters that can have a significant effect on net ion yield.

* Author for correspondence

Introduction

Matrix-assisted laser desorption / ionization (MALDI) has become a widely utilized analytical tool, yet only recently has a comprehensive understanding of MALDI with ultraviolet (UV) laser excitation begun to take form. The physical aspects of MALDI overlap considerably with the body of experiment and theory developed for laser ablation of molecular substrates. This topic has recently been extensively reviewed,[2] and Dreisewerd has considered the MALDI case in detail.[3] Molecular dynamics simulations of MALD (without ionization) by the Vertes group[4-6] and by Zhigilei, Garrison and coworkers,[7-13] have been instrumental in providing insights into the molecular level mechanism of molecular ejection in MALDI. This steady progress in understanding of desorption and ablation in MALDI has been accompanied by development of MALDI ionization models at the macroscopic continuum level. Currently the only ionization model capable of quantitative agreement with a wide range of MALDI phenomena is that of refs. [1,14-16]. The present work unifies the ionization aspects of that model with the ability of the Zhigilei/Garrison model to treat desorption and ablation .

UV-MALDI as routinely practiced spans two physical regimes, loosely designated "desorption" and "ablation." At low laser fluences, neutrals and ions are emitted individually (desorption), while above a well-defined threshold fluence, the sample decomposes more violently, leading to ejection of molecular aggregates or clusters as well as individual molecules (ablation). These clusters have been indirectly[17-19] and directly[20,21] observed, and predicted by MD simulations.[7,8,10]

The transition from desorption of individual molecules to collective material ejection (ablation) has been found to be defined by thermodynamic and/or photomechanical driving forces.[9] Thermodynamics dominates in the regime where local energy deposition by the laser is fast compared to energy redistribution by thermal diffusion. This is known as thermal confinement. In this case, the ablation threshold fluence is determined by the critical energy density for the overheating of the surface layer above the limit of its thermodynamic stability. Normal surface evaporation (desorption) then turns into an explosive transition of the overheated surface layer to a mixture of vapor and liquid droplets (ablation).

Photomechanical effects driven by the relaxation of laser-induced stresses can also result in disintegration and ejection of large droplets or chunks of material at energy densities much lower than those required for boiling and vaporization.[7-9,11] The magnitude of the laser-induced stresses and the role of the associated

photomechanical effects in the material ejection become significant under conditions known as stress confinement, when the laser pulse duration is shorter then the time needed for mechanical relaxation (expansion) of the absorbing volume. Conventional nanosecond UV-MALDI typically corresponds to thermal confinement, and photomechanical effects are unlikely to contribute significantly to material ejection. Partial or full stress confinement may occur in IR-MALDI and sub-nanosecond UV-MALDI. The results presented here suggest that electronic relaxation processes in the matrix material can significantly slow the conversion of the deposited laser energy to heat, reducing the contribution of photomechanical effects even in the case of picosecond UV-MALDI.

The fraction of ablated or desorbed material which is detected as ions in UV-MALDI is rather small. Estimates are in the range of 10^{-5} to 10^{-3}.[3,22,23] Numerous ionization mechanisms have been proposed,[17,24-28] ranging from "preformed" ions to single molecule events to those involving large clusters.

While different ionization mechanisms may be active in different circumstances, and in different matrices, to date only one ionization model has demonstrated quantitative predictive ability and agreement with diverse MALDI data.[1,14-16] The model integrates rate equations for matrix and analyte neutral and ion states in a continuous material, including the expanding plume. The primary ionization pathway is energy pooling by two excited matrix molecules.[15] Long known in condensed phase,[29-32] pooling is a result of the relatively strong interactions between aromatic pi-electron systems when packed closely in the condensed phase. Using fluorescence quenching and MALDI time-delayed 2-pulse data,[33,34] empirical rate constants for pooling processes were determined. Recently it was demonstrated that excitations are mobile in at least one matrix (2,5 dihydroxybenzoic acid),[35] so these rates are a superposition of direct and indirect processes.

The most serious limitation of the rate equation approach is that it makes assumptions about the transition from the solid to fluid phase. This was initially treated as a step function at the sublimation temperature. When a layer of the solid sample reached this temperature, it was assumed to become a homogenous gas, expanding adiabatically into the vacuum. A proportional post hoc correction was made for any fraction of material ejected in condensed form (assumed not to contribute to free ions at the detector). Because vapor pressure increases exponentially with temperature, this approximate model functioned sufficiently well to yield useful results.

Nevertheless, questions remained regarding the phase transition and its effect on ion yield. The present work addresses this gap using molecular dynamics (MD), removing the need to impose any assumptions on this aspect of the MALDI model. Of course, MD brings its own limitations with it, but these are less restrictive and arbitrary than those of the step function phase change.

It is important to note that MALDI-relevant processes can extend to tens or even hundreds of nanoseconds after the laser pulse, beyond the range of practical MD simulations. This is a consequence of the density and expansion characteristics of the ablation/desorption plume.[14,16] However, this is mostly relevant for secondary ion-molecule reactions leading to analyte ions.[16-19,27] It has also been successfully described by conventional continuum models for the plume expansion and the appropriate reaction rate equations.[1] Here we are only concerned with primary matrix ionization and the early time range, for which analytical descriptions are lacking. The MD model is intended to illuminate the most dynamic and least understood part of MALDI, not to replicate the complete event.

In order to extend the time and length scales accessible for MD simulations into the range necessary for an adequate representation of collective material ejection in laser ablation, a coarse-grained MD technique, dubbed the breathing sphere model, has been developed. This model has yielded a wealth of information on the microscopic mechanisms of laser ablation, the parameters of the ejected plume (velocity distributions of matrix and analyte molecules and cluster ejection), and their dependence on the irradiation conditions.[7-11] The breathing sphere model has been recently extended to include a description of photochemical processes, such as photofragmentation of excited molecules, formation of radicals and subsequent abstraction and recombination reactions.[7,8,12,13] Ionization processes, however, have not previously been included in the breathing sphere model. Ionization is exactly the part of MALDI that makes it useful as an analytical tool and progress in understanding of the ionization mechanisms could make a direct impact on practical applications. Here, that gap is filled by incorporating a description of ionization mechanisms, previously used in the continuum model,[1] into the MD simulations. The combined model provides new insights into the interaction of physical processes of the laser-induced phase transitions with photochemical processes leading to generation of ions in MALDI.

Computational Methods
Breathing sphere model

The breathing sphere model is described in detail in Ref. [7] and earlier publications. Briefly, the model assumes that each molecule (or an appropriate group of atoms) can be represented by a single particle (here of mass 100 Da) that has the true translational degrees of freedom but an approximate representation of internal degrees of freedom. The parameters of the interparticle interactions are chosen to reproduce the van der Waals interaction in a molecular solid with a cohesive energy of 0.6 eV, an elastic bulk modulus of ~ 5 GPa, and a density of 1.2 g/cm^3. The single internal degree of freedom, a breathing mode, is implemented by allowing the particles to change their sizes. The breathing mode also is the recipient of energy released by internal conversion from electronically excited states. The potential function of the internal motion controls the rate of the energy flow between the vibrationally excited molecules and the surrounding molecules. Since molecules rather than atoms are the particles of interest in the model, the system size can be large enough to model collective dynamics leading to laser ablation and and sample disintegration. Moreover, since explicit atomic vibrations are not included, the time step in the numerical integration of the equations of motion can be relatively long. Simulations as long as nanoseconds thereby become feasible.

A computational cell of 10 X 10 X 360 nm (255,744 molecules) was used for most of the simulations reported. Periodic boundary conditions were imposed in the directions parallel to the surface, to simulate a laser spot diameter much larger than the laser penetration depth. In order to test the effect of the lateral size of the computational cell on the simulation results, an additional, larger, simulation with lateral dimensions of 20 X 20 nm (1,022,976 atoms) was performed. At the bottom of the computational cell a dynamic boundary condition is applied to account for non-reflecting propagation of the laser-induced pressure-wave through the boundary.[36]

A timestep of 5 fs was used for integration of the MD equations of motion. The cutoff radius for calculation of nonionic intermolecular interactions was 1.0 nm between the edges of the breathing spheres. The list of neighbors for each molecule was updated every 25 time steps. The neighbor list radius was the cutoff radius plus 0.25 nm.

Excited states and ionization

To add ionization to the MD model, excited electronic and ion states of the matrix must be included. A popular and well characterized MALDI matrix is 2,5

dihydroxybenzoic acid (DHB). This matrix is modelled here, as in the continuum treatment.[14]

As seen in Fig. 1, pooling ionization mechanisms include at least three states of the matrix: the ground electronic (S_0) and two excited electronic states. The first excited state (S_1) has been well characterized by spectroscopy, and lies at 27957 cm^{-1} (3.4662 eV) in the gas phase.[37] Here it is taken to have the same energy as a single UV laser photon. The higher state (S_n) is simply one laser photon higher than the S_1, but below the ion state. Typical UV-MALDI laser wavelengths are 355 nm (3.49 eV, tripled Nd:YAG laser), or 337 nm (3.68 eV, N_2 laser), so two photon states are indeed below the ionization potential of DHB at 8.054 eV.[37]

Although ionization energies decrease in clusters and condensed phases, the scheme of Fig. 1 is expected to apply at all times for DHB. IP reductions have been studied as a function of DHB cluster size, showing an apparent asymptotic large size limit of around 7.8 eV.[38] Analysis of electron emssion data also led to the conclusion that 2-photon ionization of DHB is possible for thin films on metals, due to surface states, but remains 3-photon in thick films typical for MALDI.[39] Calculations have also predicted that even DHB anions will have quite high electron detachment energies (8.5 eV, above the free molecule IP) in the solid phase, although they are smaller for clusters.[40] Ionization in solid DHB is therefore not believed to be possible with the energy of two typical laser photons. The position of the IP above the 2-photon energy determines the amount of electronic energy converted to heat in an ionization event, but this is small compared to nonradiative relaxation of excited states. The precise value of the IP in each ionization event is therefore not a critical simulation parameter.

The cross section for S_0 to S_1 excitation in the solid matrix has been the subject of various investigations.[35,41,42] We use here a reciprocal absorption coefficient of 350 nm, corresponding to a cross section of 4×10^{-18} cm^2. The S_1 to S_n cross section is taken to be twice as large. Since the depth of the computational cell was 360 nm, the laser pulse was attenuated by more than 1/e at the base of the cell. This ensured that a substantial layer at the bottom did not ablate at the fluences used.

The laser pulse was spatially uniform across the irradiated face of the sample. Photons entered the sample at normal incidence, along the Z axis. Photon absorption was based on the Z position of the molecules. For each impinging

photon, the molecules are sequentially given a chance to make an absorption, starting at the top. At low laser intensity this yields a Beer's law (exponential) excitation profile vs. depth in the sample. At high laser intensity, as can occur in MALDI, the profile is flatter due to "bleaching" of the upper layers. In the present simulations, sub-exponential excited state distributions occur in the upper 10-15 nm of the sample, at the peak of the laser pulse.

In all simulations shown here, a Gaussian temporal laser pulse width of 30 ps was used. The laser wavelength was 355 nm. These parameters correspond to a mode-locked, frequency tripled Nd:YAG laser such as that used in time resolved studies of MALDI ion generation.[34] The pulse width is also in the range which led to strong stress confinement in simulations which did not include long-lived electronic excited states.

S_1 fluorescence lifetimes in both the solid and gas phase have been measured. In a molecular beam the S_1 lifetime is 30 ns,[37] which is taken here to be the intrinsic radiative lifetime. In the solid it is in the range of 0.5-1.5 ns.[33,35,43] In the MD model, fluorescence lifetime shortening by nonradiative decay occurs as a result of collisions. A $1/R^6$ interaction potential was used, corresponding to dipole-dipole Interactions. The scaling factor for collision induced decay was adjusted to give a solid state S_1 lifetime at low excitation density of around 1.5 ns.

The nonradiative decay rate from the S_n state to the S_1 was estimated in the development of the continuum model.[14] The value selected here, $1/(20 \text{ ps})$, is similar. This is dominated by intramolecular processes due to the high density of states at the S_n energy (Kasha's rule), and was therefore taken to be unaffected by collisions.

As shown in ref. [35], matrix excitations are mobile in the DHB condensed phase. Here, the rate of energy transfer (exciton hopping) between a molecule in the S_1 and a neighboring S_0 molecule was assumed to be determined by isotropic dipole-dipole interactions. This again leads to a $1/R^6$ dependence on intermolecular separation. The scale factor for this interaction was selected to give a hopping time similar to the 50 ps found in ref. [35]. This was tested by creating a dense layer of excitations near the surface of the sample and observing the rate at which the excitation front diffused downward. The time dependent mean diffusion distance is
$D(t) = d_h(t/t_h)^{1/2}$, allowing estimation of the effective hop time, t_h. (d_h=the distance of a single hop, the mean intermolecular distance).

Pooling processes were also taken to be based on dipole-dipole interactions. Two kinds of pooling were included: $S_1 + S_1 \rightarrow S_0 + S_n$ and $S_1 + S_n \rightarrow S_0 +$ ion. The coefficients were empirically adapted using test simulations to give excited state and ion generation rates comparable with those determined for the continuum model. The $S_1 + S_n$ rate was held at a value 10 times higher that that of the $S_1 + S_1$ rate.

The collisional and dipole-dipole interactions are defined by the distances between the edges of the spherical particles (breathing spheres) rather than their centers. This approach is based on the physical concept that intermolecular interactions are governed primarily by the interaction among atoms on the exterior of the molecules.[44]

Following an $S_1 + S_n$ pooling event, one of the two molecules becomes ionized. The low energy electron released by this positive ion has a long mean free path. From the capture cross sections (1.135×10^{-16} cm^2 for DHB[45-47]) this is around 10 nm in the solid. Since this is on the same order as the simulation dimensions, electrons were assumed to move ballistically, no scattering was considered. From the point of generation a random direction was selected and the electron propagated. Capture may occur as the electron comes close to neutral molecules on this path. If capture does not occur within the simulation volume, periodic boundary conditions in the lateral dimensions are applied, and the electron propagated further. This process is continued until the electron is captured or it escapes the simulation volume vertically. Electrons escaping from the top of the simulation are recorded as such, those escaping from the bottom are implicitly captured in the underlying material. The mean distance to capture was found to be around 10 nm, as expected from the cross section.

Interionic Coulomb forces and potentials were screened. A relative dielectric constant of $\varepsilon_{bulk}=30$ was used in the initial solid phase. This was scaled by the relative local density around each ion at later times, decreasing to 1 for isolated ions. Relative local density was defined as the number of nearest neighbors (N_{local}, as determined for the MD force and potential calculations) divided by the initial average number of neighbors before laser irradiation, N_{ave}.

$$\varepsilon_{local} = 1 + \left(\varepsilon_{bulk} - 1 \right) \left(\frac{N_{local}}{N_{ave}} \right)$$

Due to the long range of the Coulomb force and small lateral cell dimensions of 10-

20 nm, simple periodic boundary conditions could become inadequate in some cases, particularly for free, unscreened ions. For calculation of interionic interactions, extended boundary conditions were therefore used. Each individual ion interacts not only with ions in the original volume, but also ions in 8 replicated volumes surrounding it in the X and Y lateral directions. This provides a more uniform electrostatic environment for all ions than conventional periodic boundary conditions. Test calculations were also performed with 2 replicated cells in each direction (24 replicates, 25 total volumes). The change in net forces and potential energies was small, below 1%. This is because of screening and overall near zero net charge density, so Coulomb forces and potentials are dominated by relatively nearby ions.

The vertical size of the simulations was larger than the lateral dimensions, especially at later times after material has been ejected at considerable velocity. Since the vertical dimension exceeds the effective Coulomb range at all times, it is possible to reduce the number of pairwise electrostatic calculations by introduction of a vertical cutoff distance. Interionic interactions are only calculated for ions that are within this Z distance of the ion in question. From examination of forces and potentials vs. Z distance at different times in test calculations, a value of 50 nm was selected as a conservative cutoff. This is larger than the average distances included in the replicated lateral volumes.

Ion recombination is an important part of the MALDI process. Many more ions are initially created than are finally released into the vacuum. Recombination is expected to occur at a distance larger than the contact distance of the molecules, via tunneling. "Contact" is here defined as the sum of the breathing sphere radii. Since the contact distance is much less than the equilibrium distance, it corresponds to a very high intermolecular energy, which is never attained in the simulations. Recombination is assumed to take place if ions approach to within a threshold multiple (typically 1.5 - 2) of the contact distance. This threshold is not a fixed absolute distance because the breathing vibrations change the instantaneous values of the molecular radii, but for no breathing, the contact distance is 0.28 nm. Since equilibrium distances in the solid are about 0.58 nm, recombination generally occurs when ions become nearest neighbors.

Electronic energy is converted to vibrational internal energy by nonradiative S_1 or S_n internal conversion and ion recombination. This energy is transferred to the

breathing mode of the molecule(s) involved, which may convert it to heat via intermolecular interactions over time. In the present model the characteristic time scale for intramolecular to intermolecular energy transfer is on the order of 20 ps.

Results and Discussion

DESORPTION AND ABLATION

Time dependent populations of DHB matrix excited and ion states are shown in Fig. 2 for a computational cell of 10 X 10 X 360 nm, containing 255744 molecules. The laser fluence was 40 mJ/cm^2. The overall form of the curves is quite similar to that obtained with the continuum model.[14] As the S_1 excitation density rises, pooling leads first to a significant population of S_n excitations, then to ions generated by $S_1 + S_n$ pooling. After this period of high reactivity, S_1 and especially S_n populations are depleted, reducing the rate of second order processes. The S_1 decay therefore flattens.

Energy storage in excited states combined with energy flow via S_1 exciton hopping is a key difference between the present model and earlier MD studies of MALDI. It buffers energy conversion from laser photons to heat, and hence increases the time scales of melting, vaporization and ablation. Conversely, the temperature and physical state of the material directly affect the time scale of collisional processes and hence excited state decay, leading to strong feedback between internal and external degrees of freedom.

Figure 3 shows snapshots of two simulations, taken at a relatively long time (1800 ps) after the laser pulse. At the lower fluence (30 mJ/cm^2) molecular ejection is well described as desorption. Individual molecules and ions are emitted from the hot surface. At higher fluence (40 mJ/cm^2), the onset of desorption is quickly followed by disintegration of a relatively thick surface region and ejection of both individual molecules and large aggregates or clusters. The gas between the clusters is quite dense and many collisions occur. This is well described as ablation, so the ablation threshold for this simulated matrix material lies between 30 and 40 mJ/cm^2.

The layered structure of the ablation plume in Fig. 3 is a consequence of the limited lateral size of the computational cell. Periodic lateral boundary conditions prevent formation of long wavelength instabilities on the surface, which are necessary for subsequent local thinning of the layer and separation of a cluster from its neighbors. Ejection of individual spherical droplets and clusters was shown in earlier simulations of laser ablation performed with the breathing sphere model and significantly larger lateral dimensions.[10] Doubling the lateral dimensions (and quadrupling the number of molecules) of the present model also leads to slightly more discrete cluster formation, as seen in Fig. 4. The large difference in lateral and axial scales in the

figures also enhances the flattened appearance of clusters in the ablation plume.

Figure 4 also shows the typical development of top layer clusters in an ablation event. Vapor bubbles which become large enough to see in these images generally continue expanding to the lateral dimensions of the simulation. Since the sample is liquid well before large bubbles exist, the accelerating condensed material does not retain its initial shape. As early turbulence gives way to a relatively uniform expansion, surface tension smooths the ablated regions into droplets and clusters.

The time evolution of some physical quantities in these simulations is shown in Figs. 5 and 6. The property of interest is calculated by laterally averaging axial layers. Pressure is defined via the virial equation, and temperature is calculated from radial components of molecular velocities, to avoid contribution from the non-thermal axial stream velocity. In both simulations the conversion of electronic energy into heat results in the buildup of compressive stresses in the surface region of the sample. The compressive pressure wave propagates downward through the non-reflecting boundary at the bottom of the computational cell. The relaxation of the initial compressive stresses near the free surface of the sample also leads to the appearance of an unloading tensile wave that follows the compressive wave.

At low fluence (Fig. 5), the material first expands as electronic energy is converted to heat. Density decreases and the material melts from the surface downward. Although the initial sample is generated by fast cooling from a liquid state and has an amorphous structure, the temperature increase in the deep parts of the sample which do not melt has an "annealing" effect, inducing partial crystallization of the metastable amorphous structure. Several high density crystallites are visible in Fig. 5a at depths exceeding -180 nm, the uppermost ones melt toward the end of the simulation. The crystalline regions extend throughout the computational cell in the lateral direction, leading to compressive quasi-static anisotropic stresses that cannot relax by unidirectional expansion in the Z direction (the sizes of the computational cell in the lateral directions are fixed).[11] As a result, the crystalline regions can be also identified in the pressure plot, Fig. 5b, as regions of discontinuously elevated pressure within the pressure waves propagating from the surface.

In Fig. 5, evaporation at the surface is uniform, and after 500 ps the gas is sufficiently dense that numerous collisions occur, as is apparent from trajectories of individual ions in Fig. 5d. The evaporated molecules are somewhat cooler than the bulk, their temperature corresponds to that of the surface, which is cooled by the

evaporation. A transient void appeared at about 600 ps and 150 nm below the surface (see Fig. 5a). As seen in Fig. 5b, the appearance of this void is correlated with the passage of the tensile unloading wave.

In the higher fluence simulation (Fig. 6) the material also expands thermally and melts, but looses structural integrity in the top several tens of nm at about 350-400 ps. This appears to be more a thermal than a stress event. The tensile stresses are low at the time of disintegration, and the temperature is around 1000 K. Several small clusters are ejected at velocities proportional to their original depth. Some further disintegrate in the plume, which is clearly a thermal process, since no tensile stresses are present at longer times. In general, ablation in the top 100 nm of the material can be largely described as thermal at this fluence. The edges of the top clusters are initially indistinct, but later are well defined and do not change thickness over the remainder of the simulation. The ablation of the top 100 nm of the material can be largely described as an explosive decomposition of the overheated matrix into liquid droplets and vapor. Note that the phase explosion does not involve nucleation and growth of well-defined vapor bubbles and, therefore, the timescale of the ablation process is not limited by slow kinetics characteristic of the evolution of vapor bubbles in homogeneous boiling. As discussed earlier,[10] material overheated above the thermodynamic critical temperature undergoes a homogeneous expansion (and associated cooling), the appearance of small-scale density fluctuations leading to the formation of a foamy transient structure of interconnected liquid regions, and subsequent decomposition of the foamy structure into a mixture of liquid droplets, gas phase molecules, and small clusters. Overheating becomes weaker with increasing depth and the driving force for the thermal disintegration decreases.

Deeper in the material, the pronounced tensile wave generates several voids at about 500 ps, causing eventual liftoff of two thick clusters. Continued elastic oscillations in these clusters are observed, but no further disintegration. In view of the quite low temperatures at the depth of void generation, this process of ejection of the large layers of material can be described as photomechanical spallation.

The velocities of the ejected clusters are apparent from the slopes in Fig. 6. The initial velocities are roughly proportional to their depth of origin. The top clusters continue to accelerate at later times due to underlying gas pressure and lower layers are retarded by the same effect. Gradual conversion of electronic energy to heat continues over the time of the simulation (see Fig. 2) and supplies an additional contribution to the gas pressure. In agreement with earlier simulations,[10] the ejected

clusters initially have significantly higher temperature than the surrounding gas, but thermal equilibration by evaporative cooling is almost complete on the timescale of a few nanoseconds, Fig. 6c.

IONIZATION

The ion yield in MALDI is low in absolute terms, values of 10^{-2} to 10^{-5} have been reported.[3,22,23] The overall yield of the simulations shown is on the order of 10^{-3}. Considering only the material which has a positive net axial velocity at 2 ns, it is 8.4×10^{-4} and 1.6×10^{-4} for the high and low fluence data of Fig. 3, respectively. The simulations are consistent with experiment in this key result, and it is not necessary to invoke any "preformed" ions to achieve the correct ion yield.

The charge distributions in desorption and ablation simulations are shown in Fig. 5d and 6d. As the excited state populations reach high values shortly after the laser pulse, ion formation also becomes rapid (see also Fig. 2). Although ions are formed throughout the simulated volume, the charge density is much higher near the top, due to laser attenuation and the non-linear nature of ion forming pooling processes.

Initially the material is solid, molecular mobility is low and recombination is limited to those pairs which are accidentally nearby. As mobility increases in the upper layers, especially after melting, ion diffusion and recombination become rapid. This results in a period of relatively sudden and substantial conversion of electrostatic energy into heat. The melt front does not propagate smoothly into the material, a consequence of the random nature of laser excitation at sufficiently small scale, and the annealing effect noted above. The crystallized regions which remain solid longer than the surroundings are quite apparent in Fig. 6, as "fingers" of higher charge density.

Before recombination takes its toll, ion densities are quite high. For the total 69440 photons incident on the sample at 40 mJ/cm^2, 9832 ions exist (positive and negative) at the peak, for a quantum efficiency of 0.14. This is a lower limit, not including those ions that recombined early, or escaped electrons. For 30 mJ/cm^2, 52080 photons generated 6057 ions, for an efficiency of 0.12, only slightly less than at the higher fluence.

As recombination proceeds, only those ions remain which are sufficiently isolated from counterions that they experience relatively small net Coulomb forces. More precisely, when the mean force due to collisions and interactions with nearby

15

neutrals is as large as the net Coulomb force, ions can remain isolated. This leads to a maximum sustainable ion density in a MALDI plume, and this density depends on the local pressure and temperature.

A further factor limiting MALDI ion yield is the charge balance. Because electron mean free paths in molecular materials like MALDI matrices are on the order of 10 nm, some electrons escape from the top of a MALDI sample. This effect is apparent in Fig. 4, and was also discussed in ref. [39]. This has the consequence that the material develops a net positive charge in the top layers, which increases the net positive ion yield. The surface charge also has the interesting consequence that the first molecules emitted by the sample are positive ions ejected from the surface by electrostatic forces, shortly before neutrals are thermally emitted. These ions consequently have a high axial velocity, 4000 (30 mJ/cm^2) to 5000 m/s (40 mJ/cm^2). The leftmost regions of Fig. 4 are outside of the surface charging region, and show a more typical positive and negative charge density. As seen in Fig. 6d, this density is sustained over long times, as Coulomb forces are counterbalanced by collisions.

Ion velocities moderate quickly as emission becomes dominated by bulk vaporization. The lower panel of Figure 7 shows mean axial velocities of all molecules at 2000 ps as a solid line (40 mJ/cm^2), with the individual ion velocities superimposed as points. Apparent is the increasing stream velocity with distance from the origin. Out to 2500 nm the ions are scattered uniformly above and below the mean velocity because they are well thermalized with clusters and/or the surrounding gas. The fast early ions are already 2-3 times more distant at this time, and do not have a thermal distribution about the stream velocity. Ions desorbed from the surface at 30 mJ/cm^2 have similar velocities to those emitted from the top cluster at 40 mJ/cm^2 (400-700 m/s). This corresponds well to the ion velocity measurements of Bökelmann, Spengler and Kaufmann[48], who found fast intial ions followed by a distribution of later slower ions.

The upper panel of Fig. 7 shows the radial root mean square speeds vs axial position, compared with the axial density. Radial speeds are representative of the local temperature. In earlier high fluence simulations of laser desorption, some difference was noted between cluster temperatures and the surrounding gas, the clusters being warmer.[10] From Fig. 5c it can be seen that clusters and the gas are not fully equilibrated at earlier times. At the end of the simulations, 2 ns, equilibration is more complete, although the interior of the thickest cluster remains distinctly warmer.

In the ablation regime, ejected ions exist both in the gas phase and in clusters. There is some condensation and evaporation of ions, but it is not found that ions exist predominantly in clusters, nor is it found that ions are released from clusters downstream.[17,27] For the high fluence simulation of Figs. 6 & 7, the cluster to free ion ratio is 1.3. However, the clusters appear to be quite stable, at least on the few nanosecond timescale. They remain in approximate equilibrium with the surrounding gas and experience slow evaporative cooling during the plume expansion. The total thermal energies of the clusters suggest, however, that evaporative cooling is not sufficient to significantly affect the sizes of the ejected clusters at longer times. This confirms the assumption used in the macroscopic MALDI model that clusters make a negligible contribution to the free matrix ion yield.[14] This will be a more important issue for analyte ions, since they may be preferentially ejected in clusters.[8,17,18,49]

Figure 8 shows the effect of varying two key ionization parameters. The middle plot is the 40 mJ/cm^2 result analyzed in detail above. S_1 excitations were allowed to hop, in accord with experiment, and the radius at which ion recombination was assumed to occur was set to 2.0 times the contact radius as discussed above. The other two simulations are for the same fluence, but with the indicated parameter changes. As far as the overall physical characteristics of the ablation event, there is little to differentiate them at 2 ns. With hopping, laser energy is transported slightly deeper. With a smaller recombination radius this energy is converted somewhat later to heat.

In contrast, Fig. 9 shows that these same parameters have a dramatic effect on excited state and ion populations. The net ion yield at the right edge of the figure is twice as high for the solid curve (with hopping, short radius) as for the dot-dash trace (no hopping, long radius). When excitations are immobile, they pool less often, so the S_1 state decays much less quickly (top panel). Because ions form in a more localized region when there is no hopping, the peak ion number is the lowest for that simulation (lower panel). When hopping spreads the ions over a greater depth, there is a modest increase in peak and net ion production, as apparent from the middle trace. Reducing the recombination radius has a much more dramatic effect. This is because a radius of 2 is large enough that many ion pairs recombine before the material melts. With a radius of 1.75, recombination becomes rapid only shortly before ablation begins to separate ions via energetic collisions. This raises the possibility that a short mean electron tunneling radius is an important characteristic of a good MALDI matrix.

Conclusions

A molecular dynamics model of UV-MALDI has been developed to help understand the interaction between mechanical and reactive processes in the challenging time range during and shortly after the laser pulse. It includes radiative and non-radiative decay, exciton hopping, two pooling processes and electron capture, in addition to the previously described breathing spheres. Methods were developed to handle long-range Coulomb forces and the long mean free path of low energy electrons. The excited state processes have been adapted from the macroscopic model of ref. 1, and give overall similar results. However, a much more detailed description of the feedback between expansion and ionization is achieved.

The energy storage effect of the matrix excited states significantly decreases the heating rate in the absorbing material and allows for a partial relaxation of laser-induced stresses in the surface region. In the ablation regime the ejection of the top layers is defined mainly by the thermal process of decomposition of overheated matrix whereas the disintegration and ejection of the lower layers can be described as photomechanical spallation.

Both desorption and ablation regimes are found to generate free ions. The yields correspond well with experimental estimates. Electrons escape from the top of the sample, leading to a significant surface charge. The first molecular ions emitted are ejected from this layer, by Coulomb repulsion shortly before neutral desorption begins. Later ions are entrained in the gas of neutral molecules that is in rough local equilibrium with the surface (desorption) or clusters (ablation). The fast surface ions are followed by thermalized, entrained ions, in good agreement with experiment.

Clusters are found to be stable on a nanosecond time scale. Free ions and those in clusters are about equally abundant, but it appears that most ions in clusters will not become free until far downstream, if at all.

Exciton hopping rate and the mean radius for ion recombination are shown to be key parameters that can have a significant effect on net ion yield.

Acknowledgements

References

(1)   Knochenmuss, R. *Anal.* Chem*. **2003**, *75*, 2199.

(2)   *Laser Ablation of* Molecular *Substrates*; Georgiou, S.; Hillenkamp, F., Eds., 2003; Vol. 103.

(3)   Dreisewerd, K. *Chem. Rev. **2003**, *103*, 395.

(4)   Dutkiewicz, L.; Johnson, R. E.; Vertes, A.; Pedrys, R. *J. Phys. Chem. A* **1999**, *103*, 2925.

(5)   Wu, X.; Sadeghi, M.; Vertes, A. *J. Phys. Chem. B* **1998**, *102*, 4770.

(6)   Sadeghi, M.; Wu, X.; Vertes, A. *J.* Phys*. Chem. B* **2001**, *105*, 2578.

(7)   Zhigilei, L. V.; Leveugle, E.; Garrison, B. J.; Yingling, Y. G.; Zeifman, M. I. *Chem. Rev. **2003**, *103*, 321.

(8)   Zhigilei, L. V.; Yingling, Y. G.; Itina, T. E.; Schoolcraft, T. A.; Garrison, B. J. *Int. J. Mass Spectrom. **2003**, *226*, 85.

(9)   Zhigilei, L. V.; Garrison, B. J. *J. Appl. Phys. **2000**, *88*, 1.

(10)   Zhigilei, L. V. *Appl. Phys. A* **2003**, *76*, 339.

(11)   Leveugle, E.; Ivanov, D. S.; Zhigilei, L. V. *Appl. Phys. A* **2004**, *79*, 1643.

(12)   Yingling, Y. G.; Zhigilei, L. V.; Garrison, B. J. *J. Photochem. Photobiol. A* **2001**, *145*, 173.

(13)   Yingling, Y. G.; Garrison, B. J. *J. Phys. Chem. B* **2004**, *108*, 1815.

(14)   Knochenmuss, R. *J. Mass Spectrom. **2002**, *37*, 867.

(15)   Knochenmuss, R.; Stortelder, A.; Breuker, K.; Zenobi, R. *J. Mass Spectrom. **2000**, *35*, 1237.

(16)   Knochenmuss, R.; Zenobi, R. *Chem. Rev. **2002**, *103*, 441.

(17)   Fournier, I.; Brunot, A.; Tabet, J.-C.; Bolbach, G. *Int. J. Mass Spectrom. **2002**, *213*, 203.

(18)   Kinsel, G. R.; Edmondson, R. D.; Russell, D. H. *J. Mass Spectrom. **1997**, *32*, 714.

(19)   Kinsel, G. R.; Gimon-Kinsel, M. E.; Gillig, K. J.; Russell, D. H. *J. Mass Spectrom. **1999**, *34*, 684.

(20)   Jackson, S. N.; Mishra, S.; Murray, K. K. *J. Phys. Chem. B* **2003**, *107*, 13106.

(21)   Handschuh, M.; Nettesheim, S.; Zenobi, R. *Appl. Surf. Sci. **1998**, *137*, 125.

(22)   Puretzky, A. A.; Geohegan, D. B. *Chem. Phys. Lett. **1997**, *286*, 425.

(23)   Mowry, C.; Johnston, M. *Rapid Comm. Mass Spectrom. **1993**, *7*, 569.

(24)   Ehring, H.; Karas, M.; Hillenkamp, F. *Org. Mass Spectrom. **1992**, *27*, 427.

(25)   Zenobi, R.; Knochenmuss, R. *Mass Spectrom. Rev. **1998**, *17*, 337.

(26)   Karas, M.; Glückmann, M.; Schäfer, J. *J. Mass Spectrom. **2000**, *35*, 1.

(27)   Livadaris, V.; Blais, J.-C.; Tabet, J.-C. *Eur. J. Mass Spectrom. **2000**, *6*, 409.

(28)   Liao, P.-C.; Allison, J. *J. Mass Spectrom. **1995**, *30*, 408.

(29)   Northrop, N. C.; Simpson, O. *Proc. Roy. Soc. London* **1958**, *A244*, 377.

(30)   Pope, M.; Swenberg, C. E. *Electronic Processes in Organic Crystals and Polymers*; Oxford University Press: Oxford, 1999.

(31)   Birks, J. B. *Organic Molecular Photophysics*; Wiley: New York, 1973; Vol. 1.

(32)   Birks, J. B. *Photophysics of Aromatic Compounds*; Wiley Interscience: London, 1970.

(33)   Lüdemann, H.-C.; Redmond, R. W.; Hillenkamp, F. *Rapid Comm. Mass Spectrom.* **2002**, *16*, 1287.

(34)   Knochenmuss, R.; Vertes, A. *J. Phys. Chem. B* **2000**, *104*, 5406.

(35)   Setz, P.; Knochenmuss, R. *J. Phys. Chem. A* **2005**, *109*, 4030.

(36)   Zhigilei, L. V.; Garrison, B. J. *J. Mat. Res. Soc. Symp. Proc.* **1999**, *538*, 491.

(37)   Karbach, V.; Knochenmuss, R. *Rapid Commun. Mass Spectrom.* **1998**, *12*, 968.

(38)   Lin, Q.; Knochenmuss, R. *Rapid Comm. Mass Spectrom.* **2001**, *15*, 1422.

(39)   Knochenmuss, R. *Anal. Chem.* **2004**, *76*, 3179.

(40)   Kinsel, G. R.; Zhao, Q.; Narayanasamy, J.; Yassin, F.; Rasika Dias, H. V.; Niesner, B.; Prater, K.; St. Marie, C.; Ly, L.; Marynik, D. *J. Phys. Chem. A* **2004**, *108*, 3153.

(41)   Horneffer, V.; Dreisewerd, K.; Lueemann, H.-C.; Hillenkamp, F.; Laege, M.; Strupat, K. *Int. J. Mass Spectrom.* **1999**, *185/186/187*, 859.

(42)   Allwood, D. A.; Dreyfus, R. W.; Perera, I. K.; Dyer, P. E. *Rapid Commun. Mass Spectrom.* **1996**, *10*, 1575.

(43)   Zechmann, C.; Muskat, T.; Grotemeyer, J. *Eur. J. Mass Spectrom.* **2002**, *8*, 287.

(44)   Kitaigorodsky, A. I. *Molecular Crystals and Molecules*; Academic Press: New York, 1993.

(45)   Asfandiarov, N. L.; Pshenichnyuk, S. A.; Forkin, A. I.; Lukin, V. G.; Fal'ko, V. S. *Rapid Commun. Mass Spectrom.* **2002**, *16*, 1760.

(46)   Pshenichnyuk, S. A.; Asfandiarov, N. L.; Fal'ko, V. S.; Lukin, V. G. *Int. J. Mass Spectrom.* **2003**, *227*, 281.

(47)   Pshenichnyuk, S. A.; Asfandiarov, N. L.; Fal'ko, V. S.; Lukin, V. G. *Int. J. Mass Spectrom.* **2003**, *227*, 259.

(48)   Spengler, B.; Bökelmann, V. *Nucl. Instr. Meth. Phys. Res. B* **1993**, *82*, 379.

(49)   Zhou, J.; Ens, W.; Standing, K. G.; Verentchikov, A. *Rapid Commun. Mass Spectrom.* 1992, *6*, 671.
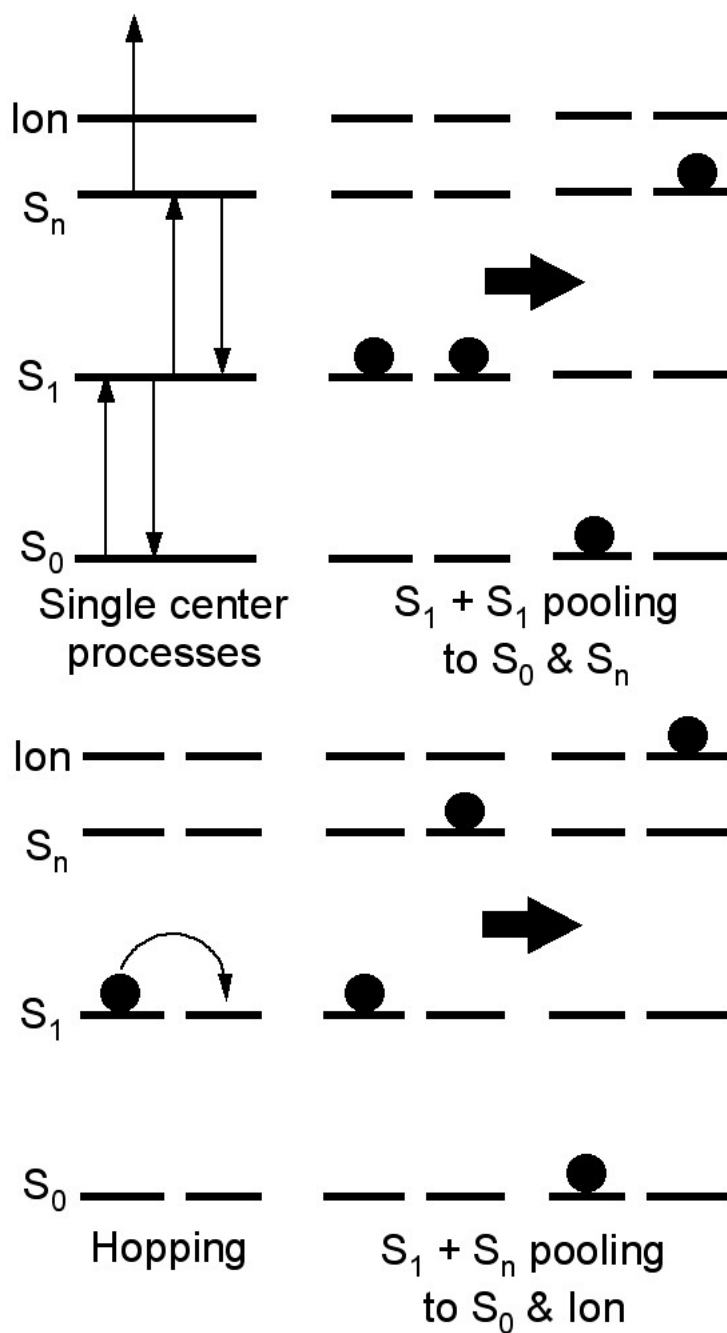
Figures

Figure 1: Schematic of the excitation, relaxation and ionization processes included in the model. The upper left panel shows the unimolecular processes. Deexcitation from the S_1 may be radiative or non-radiative. The S_n is deactivated only nonradiatively. Pooling and hopping are bimolecular processes.
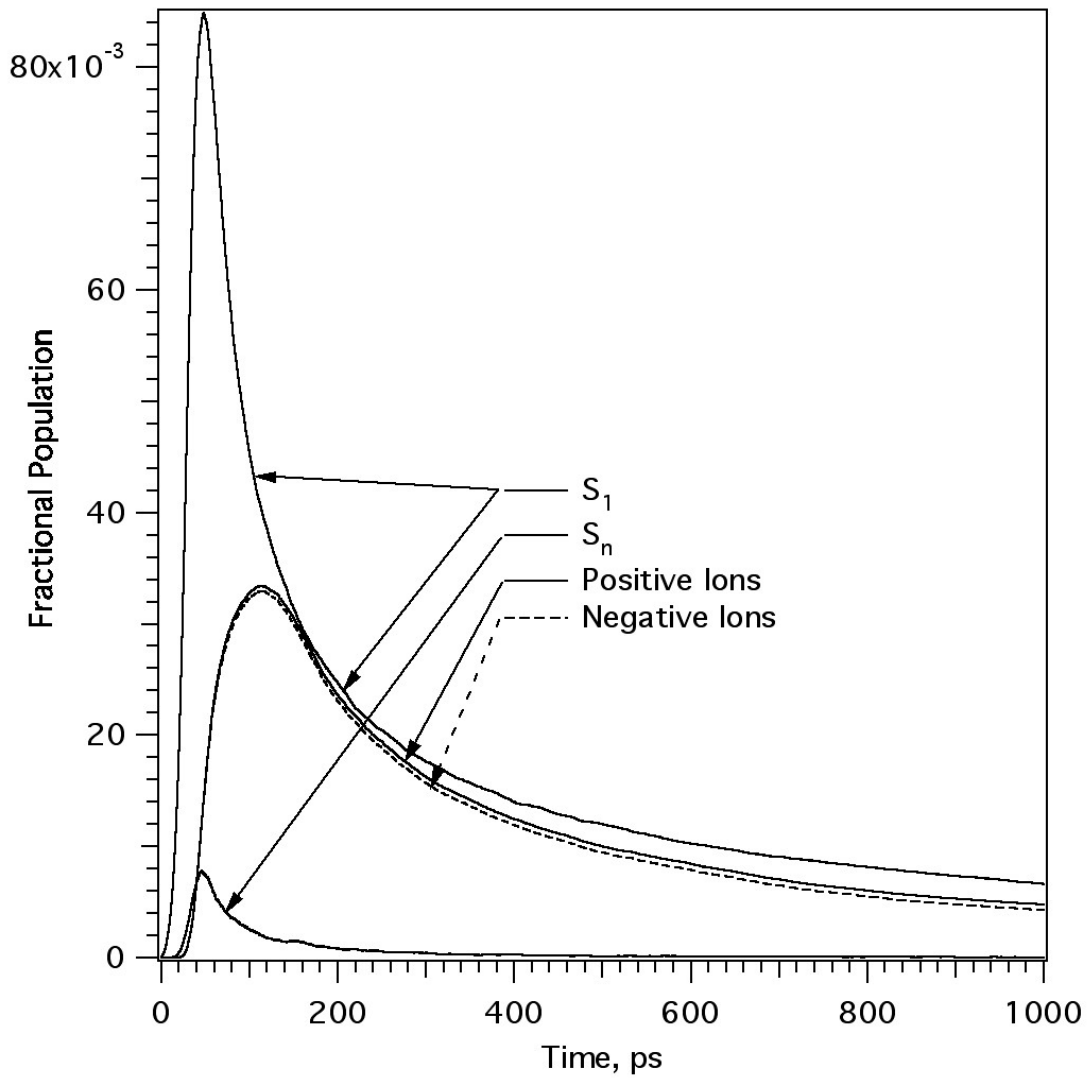
Figure 2. State populations vs. time in an MD MALDI simulation of 255744 molecules in a 10 X 10 X 360 nm volume. The 355 nm laser fluence was 40 mJ/cm^2, and the pulse had 30 ps Gaussian full width. Exciton hopping was included.
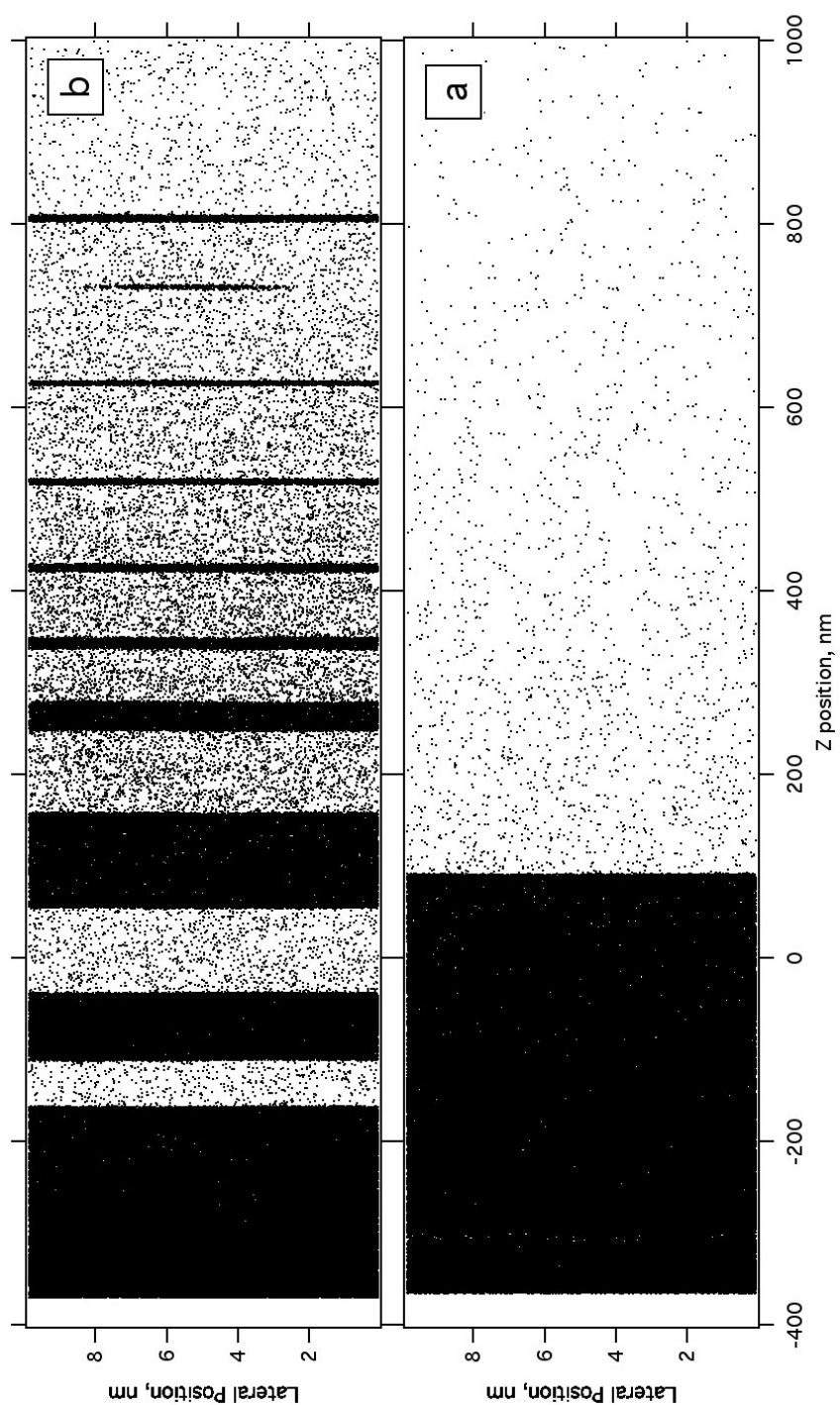
Figure 3. Snapshots of two MD MALDI simulations at 1800 ps after a 30 ps 355 nm laser pulse. The fluences were 30 (a) and 40 mJ/cm^2 (b). The low fluence event may be described as desorption, individual molecules leave the surface. The high fluence event is ablation, large aggregates are ejected as well as single molecules.

23
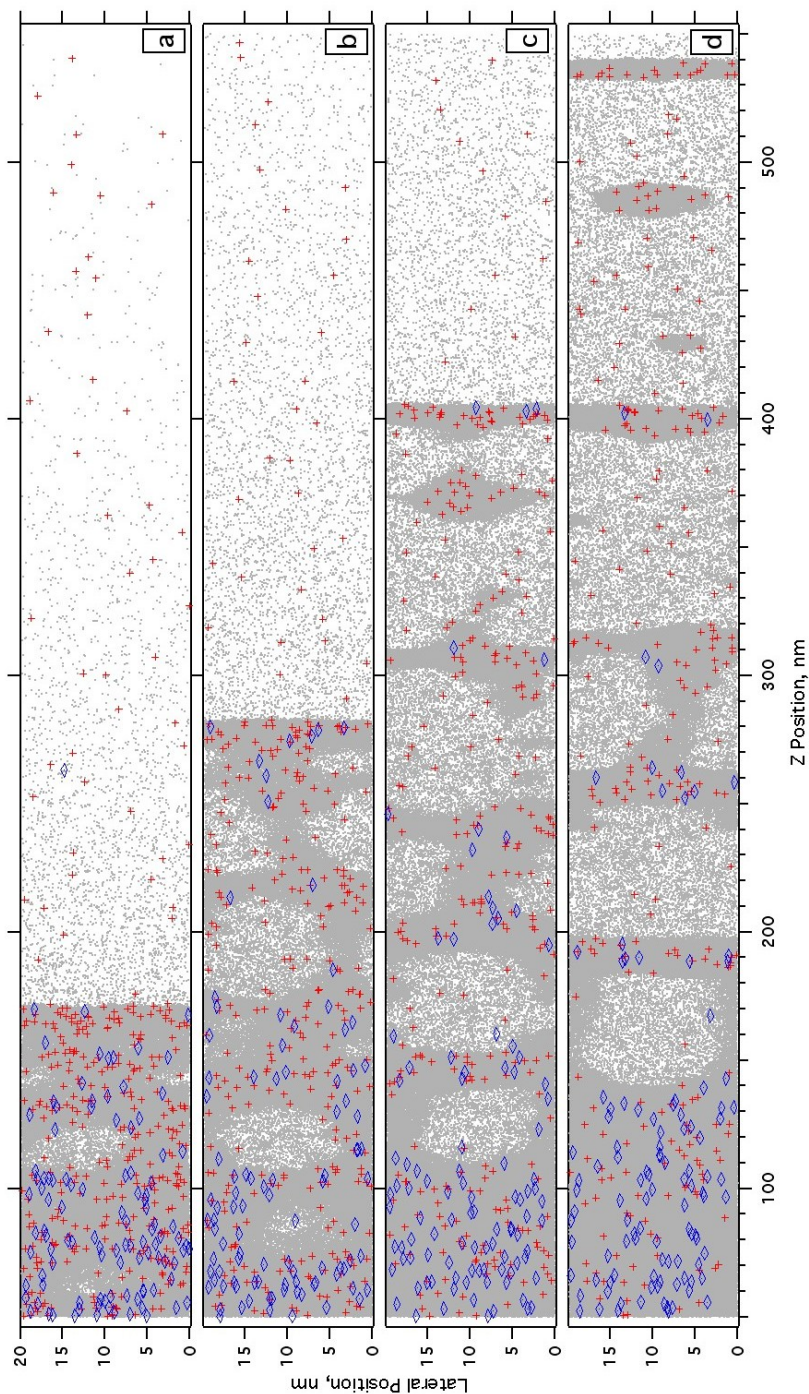
Figure 4: Snapshots of a 40 mJ/cm^2, 20 X 20 X 360 nm (1022976 molecules) simulation, showing ablation and cluster formation. From top to bottom the times were (a) 500, (b) 750, (c) 1000 and (d) 1250 ps. The 30 ps laser pulse was centered at about 40 ps. Only the top layers of the simulation are shown. Neutral molecules are denoted as gray points, positive ions as red crosses, and negative ions as blue diamonds. Note the excess of positive charge in the surface region.
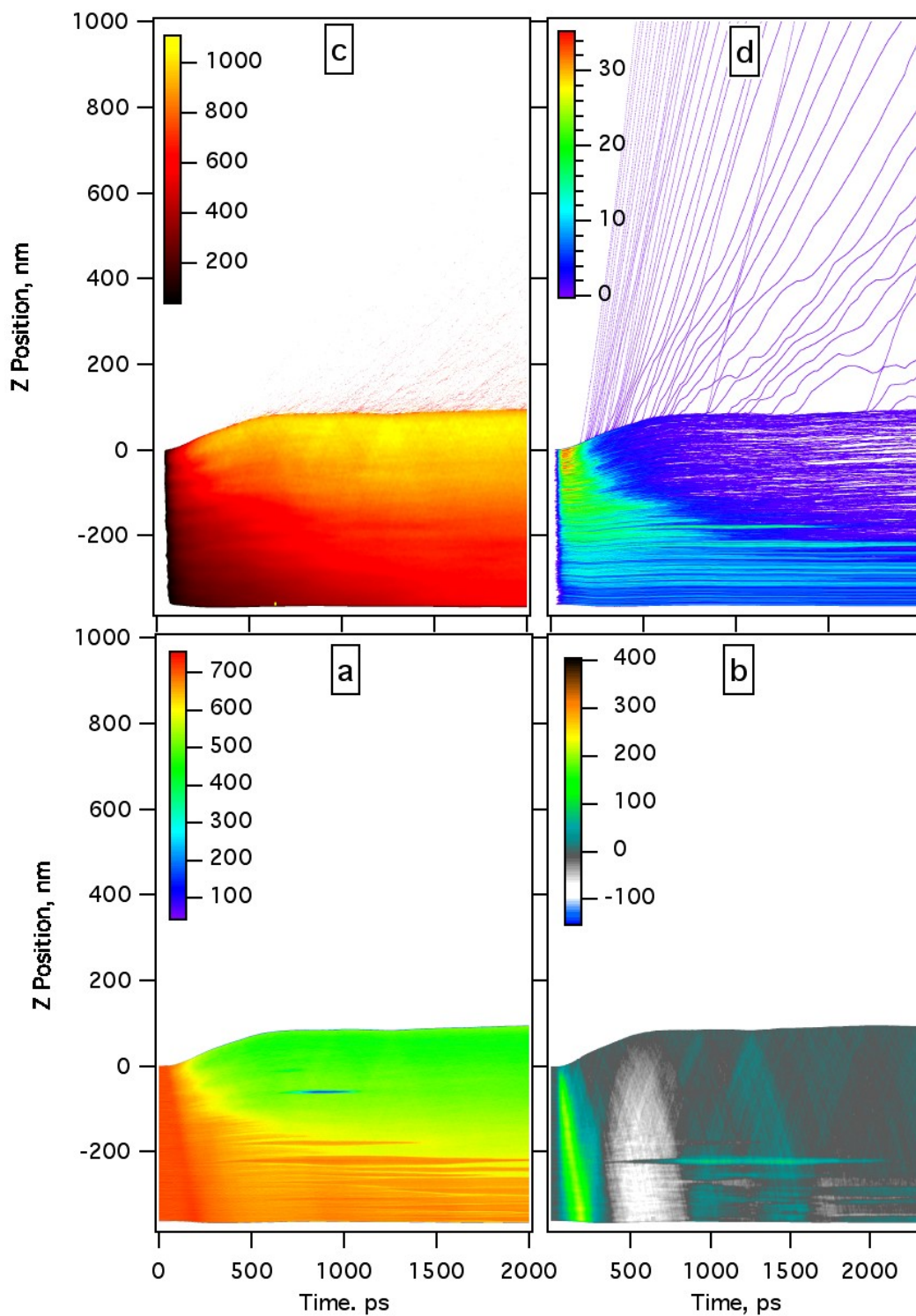
Figure 5. Properties vs time and axial position for a 30 mJ/cm², 10 X 10 X 360 nm simulation. (a) Density, molecules per nm in the axial direction. (b) Pressure, MPa. (c) Temperature, K. (d) Total charges (positive plus negative) per nm in the axial direction.
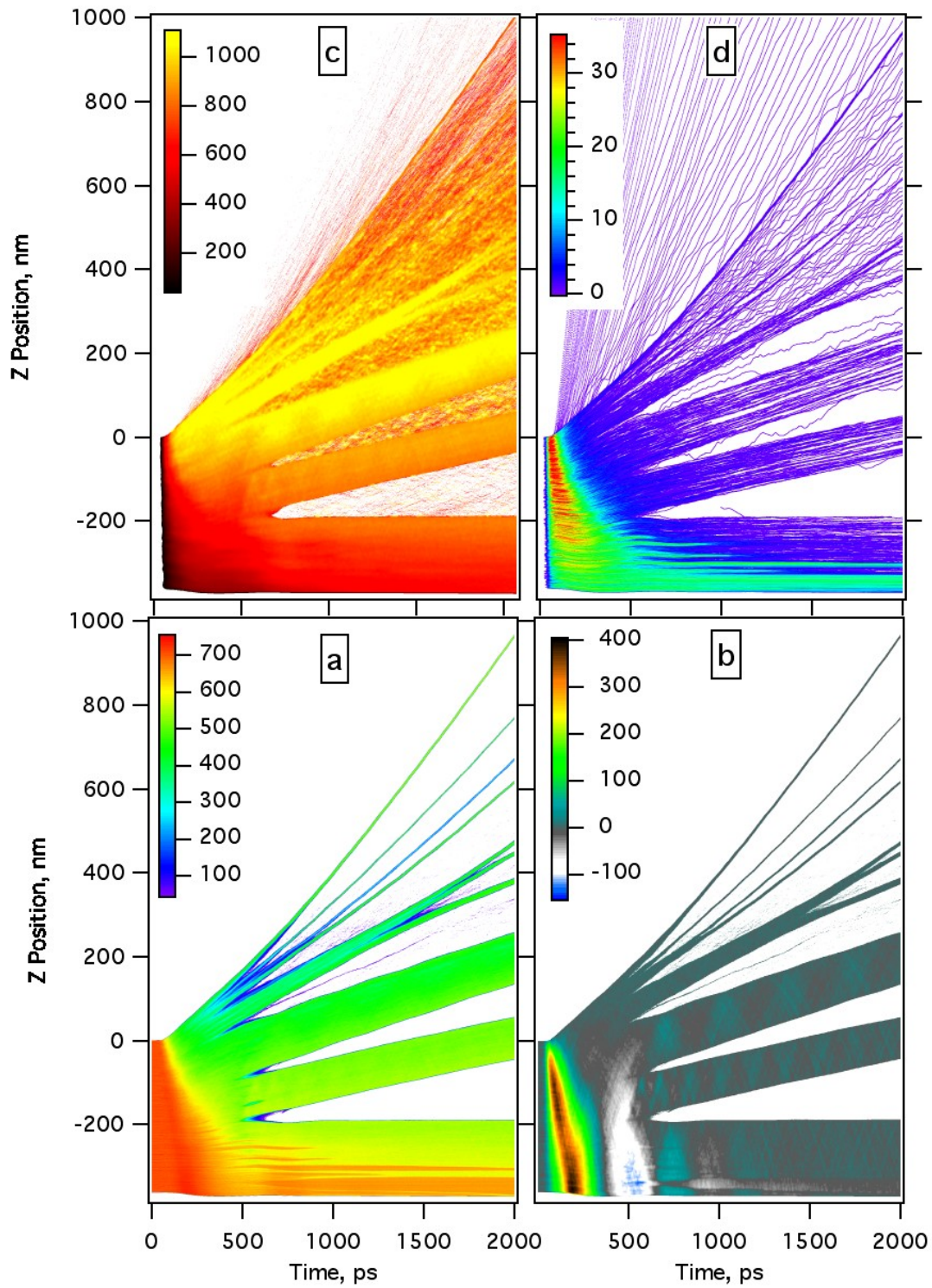
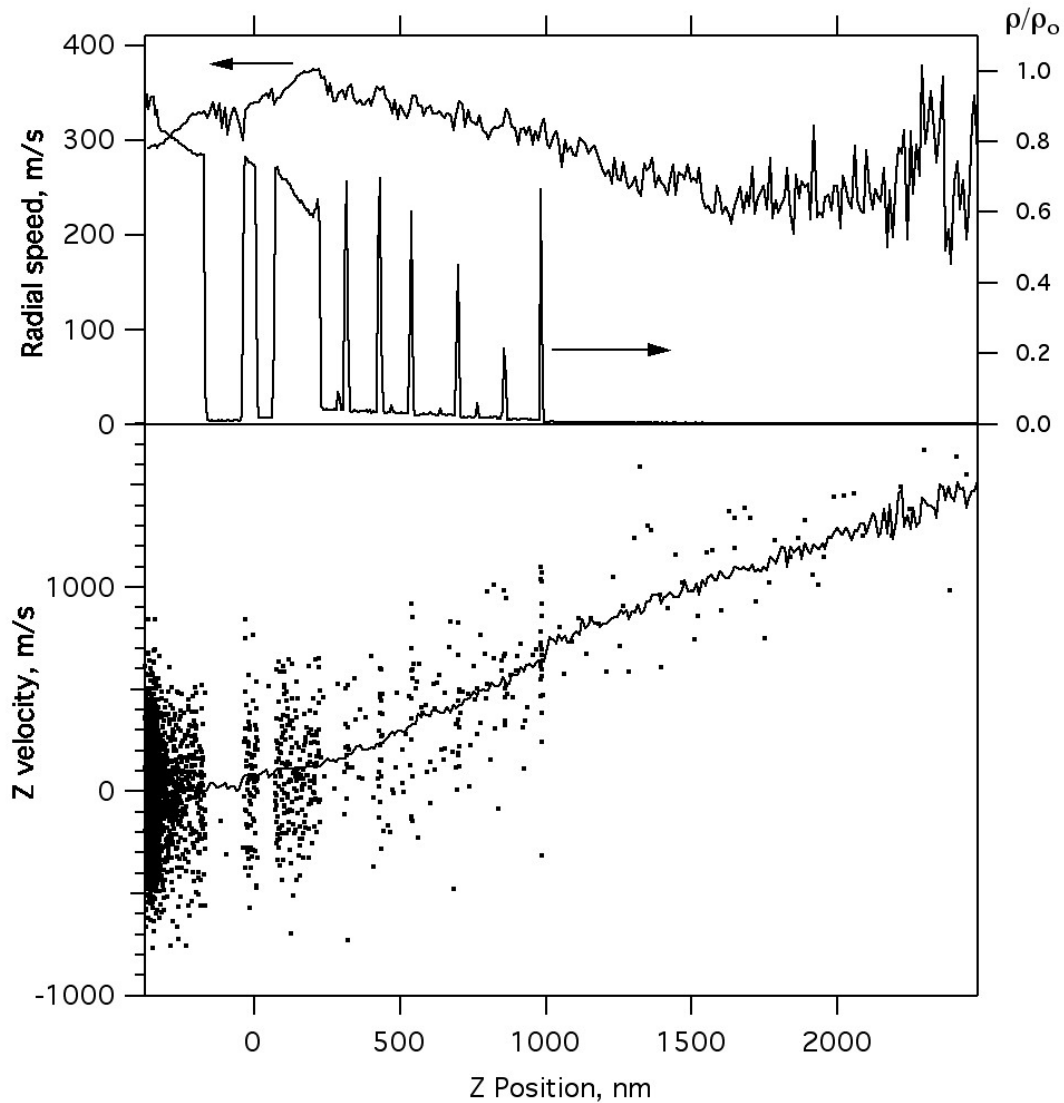Figure 6. Same as Figure 5, but for a laser fluence of 40 mJ/cm^2.

Figure 7. Velocities and densities vs axial position for a 40 mJ/cm^2 simulation at 2 ns. The solid trace in the bottom panel is a moving average of the axial velocities of all molecules. The molecules and clusters ejected earliest have the highest axial stream velocities. Superimposed as points are the individual velocities of all ions. These are symmetrically distributed about the mean velocities, indicating that the ions are entrained in and thermalized with the neutral molecules. The number of free ions is about the same as those within clusters. The top panel shows a density histogram for all molecules (right axis). The gas between clusters is still quite dense, several percent of the cluster density in some regions. The top trace (left axis) is a moving average of the radial speed of all molecules, indicative of the local temperature. With the possible exception of the thick cluster at 200-300 nm, the clusters and gas are well equilibrated.
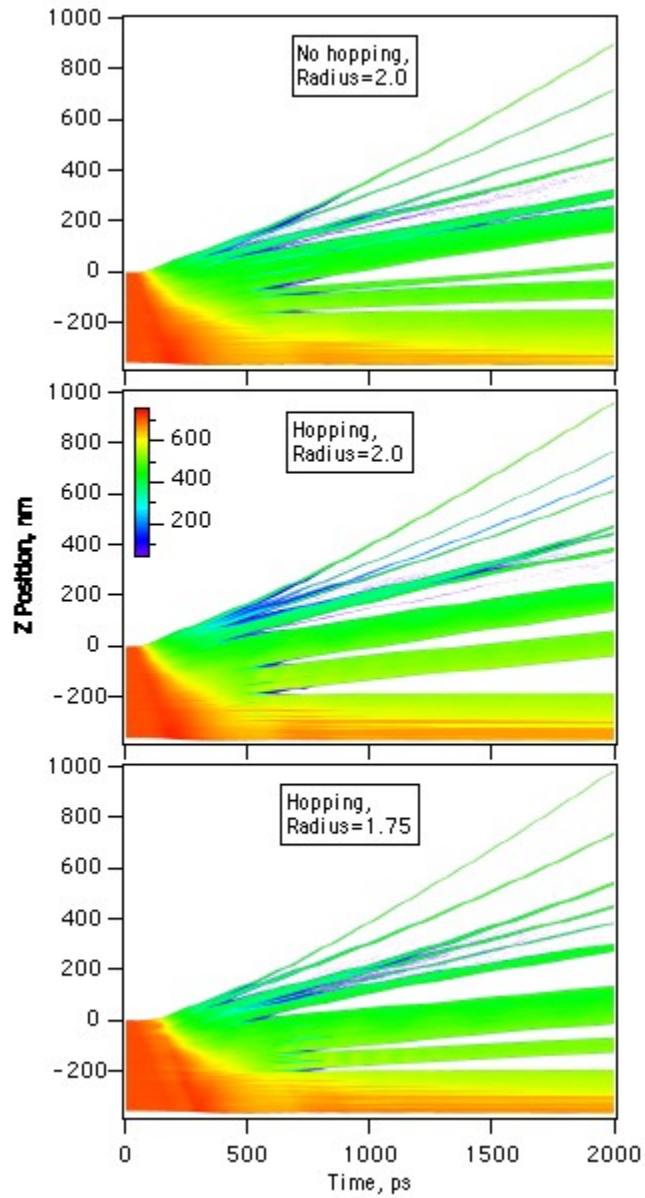
Figure 8. Density vs time and axial position for three simulations at 40 mJ/cm^2. The presence or absence of exciton hopping and the mean recombination radius were varied. There is relatively little difference in the physical characteristics of the ablation events.
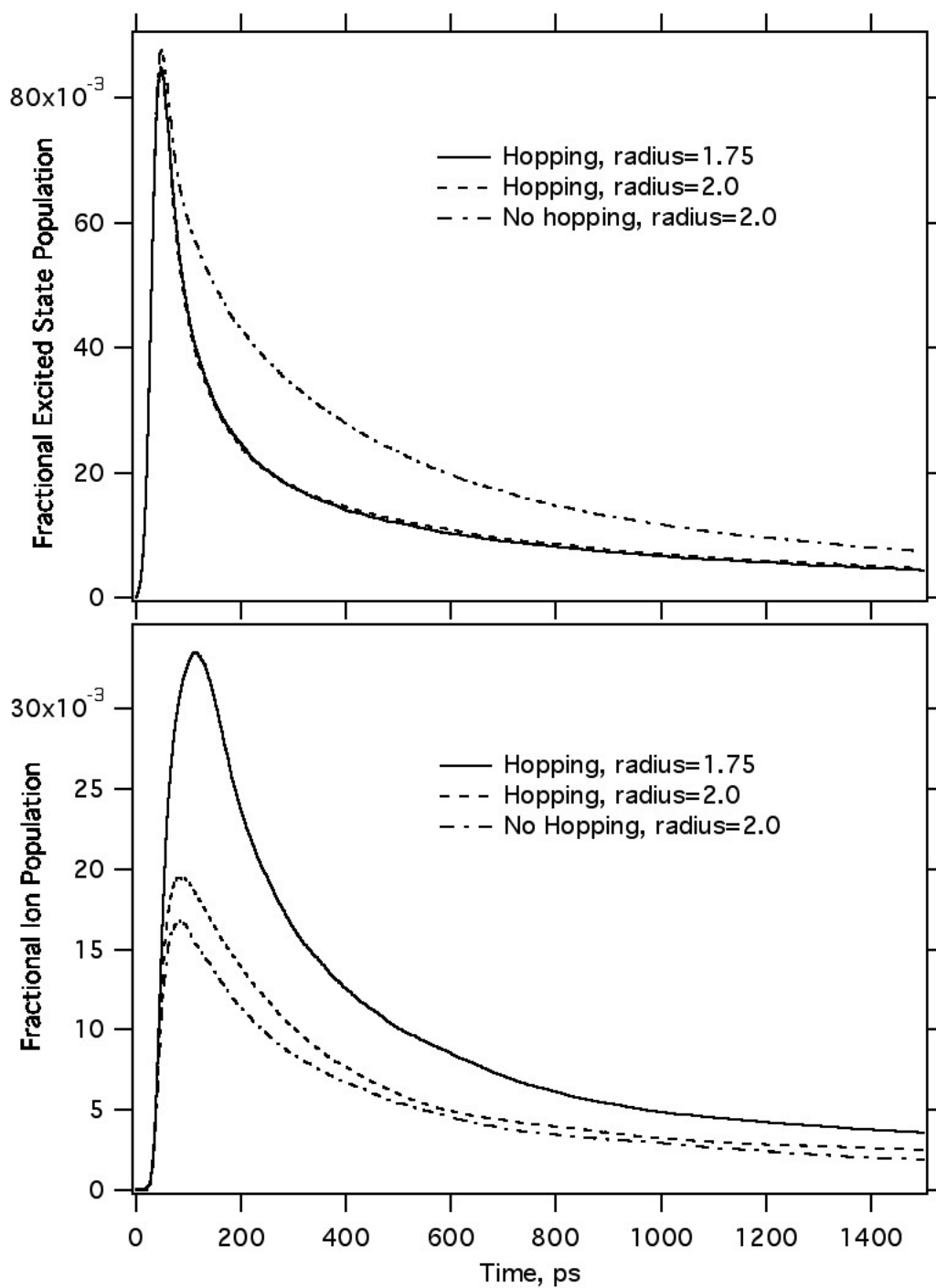
Figure 9. S_1 (upper panel) and positive ion (lower panel) relative populations for the same parameter variations as in Fig. 8. Both hopping and the recombination radius multiplier have a large effect on S_1 populations and ion yields.